FRONTIERS OF PHYSICS

RESEARCH ARTICLE
Volume 19 / Issue 3 / 33207 / 2024

Resonant four-photon photoemission from $SnSe_2(001)$

Chengxiang Jiao[1], Kai Huang[1], Hongli Guo[2], Xingxia Cui[1], Qing Yuan[1], Cancan Lou[1], Guangqiang Mei[1], Chunlong Wu[3], Nan Xu[3], Limin Cao[1], Min Feng[1,3,†]

1 School of Physics and Technology and Key Laboratory of Artificial Micro- and Nano-Structures of Ministry of Education, Wuhan University, Wuhan 430072, China
2 Department of Physics and Astronomy, California State University Northridge, Northridge, CA 91330-8268, USA
3 Institute for Advanced Study, Wuhan University, Wuhan 430072, China
Corresponding author. E-mail: †fengmin@whu.edu.cn
Received October 12, 2023; accepted October 27, 2023

ABSTRACT

High-order nonlinear multiphoton absorption is usually inefficient, but can be enhanced by designing resonant excitations between occupied and unoccupied energy levels. We conducted angle-resolved multi-photon photoemission (mPPE) studies on the $SnSe_2(001)$ surfaces excited by ultrashort laser pulses. By tuning photon energy and light polarization, we demonstrate the presence of a resonant four-photon photoemission (4PPE) process involving the occupied valence band (VB), the unoccupied second conduction band (CB2) and the unoccupied image-potential state (IPs) of $SnSe_2$. In this 4PPE process, VB electrons of $SnSe_2$ are resonantly excited into CB2 by adsorbing two photons, followed by the adsorption of another photon to populate the $n = 1$ IPs before being emitted out to the vacuum by adsorbing one more photon. This results in a double-resonant 4PPE process, which exhibits approximately a 40 times enhancement in photoemission yields compared to cases where one of the resonant pathways, CB2 → IPs, is inhibited by involving a virtual state instead of the IPs in the 4PPE. The double-resonant 4PPE process efficiently excite the bulk VB electrons outside the vacuum, like taking advantage of resonant "ladders" through two real empty electronic states of $SnSe_2$. Our results highlight the important applications of mPPE in probing the band-structure, particularly the unoccupied states, of recently emerging main group dichalcogenide semiconductors. Furthermore, the discovered resonant mPPE process contributes to the exploration of their promising optoelectronic applications.

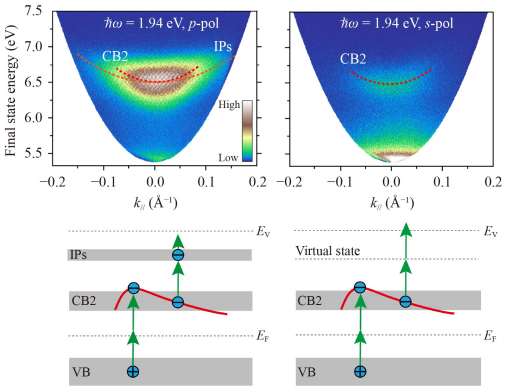

Keywords multi-photon photoemission, four-photon photoemission, $SnSe_2$, unoccupied states, resonant excitation

1 Introduction

The nonlinear photoelectric effect can be realized by multiphoton process in solids induced by ultrashort laser pulses. In these processes, the occupied initial states, the unoccupied intermediate states, and the coupling between them play a center role [1, 2]. Multiphoton photoemission (mPPE) is highly sensitive to the wave functions and energy levels of the states involved in the excitation, making it a powerful tool for observing the unoccupied band structure of materials with high energy-momentum resolution and investigating the dynamics of electronic excitations at solid surfaces [1, 3–13]. Among

Higher Education Press

https://doi.org/10.1007/s11467-023-1365-4

mPPE techniques, two-photon photoemission (2PPE) represents the lowest and most accessible order of nonlinearity. In 2PPE, the photon energy for photoemission experiments is selected to be lower than the work function (Φ) of the system, typically in the range of few electronvolts for most materials. Consequently, two photons are required to excite occupied electrons near the Fermi energy (E_F) into the vacuum. The range of accessible unoccupied electronic state is determined by the difference between twice the photon energy and the Φ, and thus is limited by the single photon energy [1]. Utilizing laser pulses with lower photon energy enables the observation of the photoemission signal for higher orders of nonlinearity through mPPE. This approach is practicable for extending the range of accessible unoccupied electronic states [6–9]. Moreover, mPPE beyond the second order would allow the observation of light-induced resonances that are not accessible through ordinary photoemission techniques such as angle-resolved photoemission spectroscopy (ARPES) or 2PPE. For instance, Bisio *et al.* [8] demonstrated high-order 3- to 4-photon photoemission involving occupied Cu *d* bands, unoccupied *sp* bands and $n = 1$ image-potential state (IPs) from Cu(001) surfaces. Winkelmann *et al.* [7] further revealed a 3rd-order resonance involving the Cu *d* bands as initial states, the *sp* bands, and IPs as the first and second intermediate states, respectively. These resonant 3PPE processes exhibit the contribution of coherent excitation pathways in photoemission.

Despite its importance, high-order mPPE from surfaces is a much less-explored field compared to conventional ARPES or 2PPE. This is mainly due to the significantly reduced photoelectron yields, which can be overshadowed by space charge effects from the low-order processes [4, 14–18]. Moreover, non-photoelectric emission through surface plasmon excitation and, possibly, tunneling can also interfere with the mPPE signal [17, 19]. As a result, high-order mPPE studies normally are limited to solids other than noble metals, which are more stable and have well-known band structures. While mPPE has recently been reported for graphite [20–22], it has rarely been performed on the emerging class of two-dimensional (2D) materials beyond graphene.

Tin diselenide ($SnSe_2$), a main group dichalcogenide sharing a layered structure similar to that of 2D graphene and transition metal dichalcogenide, has recently garnered significant interest. It has demonstrated gate-tunable interfacial superconductivity [23–28] and holds promise for optoelectronic applications [29–32]. Despite over 50 years of extensive investigation [33–43], important electronic properties of $SnSe_2$, such as the unoccupied electronic states, remain unresolved, let alone mPPE. In this paper we report the observation of a four-photon photoemission on $SnSe_2$(001) surfaces, which exhibits distinct features related to occupied and unoccupied band structures. We identify that $SnSe_2$'s valence band (VB) electrons are resonantly excited into the second conduction band (CB2) through the adsorption of two photons. This is followed by the adsorption of another photon to populate the $n = 1$ IPs, and finally, they are emitted to the final state (E_{final}) above the vacuum level through the adsorption of one more photon. This creates a double-resonant four-photon photoemission (4PPE) process: VB $\rightarrow$ CB2 $\rightarrow$ IPs $\rightarrow E_{final}$. The double-resonant 4PPE exhibits an approximately 40-times enhancement in photoemission yields compared to the VB $\rightarrow$ CB2 $\rightarrow$ Vs (virtual state) $\rightarrow E_{final}$ process, where the resonant pathway of CB2 $\rightarrow$ IPs is replaced by a non-resonant one via a Vs, rather than the IPs, in the penultimate step. The experimental results clearly demonstrate that by taking advantage of resonant excitations through two real empty electronic states of $SnSe_2$, the bulk VB electrons can be efficiently excited in the mPPE. Theoretically, we calculate the transition dipole element ($T_{n'n}$) of VB $\rightarrow$ CB2, CB2 $\rightarrow$ IPs and VB $\rightarrow$ IPs using Density Functional Theory (DFT). The estimated transition efficiency of VB $\rightarrow$ CB2 $\rightarrow$ IPs represented by $T_{VBM\rightarrow CB2} * T_{CB2\rightarrow IPs}$ is found to be much larger than that of VB $\rightarrow$ IPS ($T_{VBM\rightarrow IPs}$). This supports the idea that resonant excitation through the real CB2 intermediate state greatly enhances the excitation efficiency between the initial VB and intermediate IPs of $SnSe_2$, emphasizing the effect of real empty electronic states acting as intermediate states in mPPE.

2 Materials and methods

Sample preparation. The high-quality $SnSe_2$ single crystals used in the experiments were self-grown using the temperature gradient growth method from high-purity (99.9999%) Sn and Se granules. First, Sn and Se granules with the stoichiometry of $SnSe_2$ and a total weight of 30 g were loaded into a quartz ampoule with an inner diameter of 11 mm. Then, the quartz ampoule was evacuated to a pressure better than 5×10^{-5} Torr and sealed. The quartz ampoule was placed into a tubular furnace at a 15° angle from the horizontal plane. In the furnace, the sample was slowly heated to 680 °C over 30 h, held at this temperature for 48 h, and then gradually cooled from 680 °C to 300 °C at a precisely controlled rate of 1 °C per hour. After the furnace was cooled to room temperature (RT), the synthesized $SnSe_2$ single crystals were removed from the quartz ampoule and exposed to the air. Prior to STM, ARPES and mPPE experiments, the $SnSe_2$ crystals were cleaved *in-situ* in a preparation chamber under ultrahigh vacuum (UHV) conditions at room temperature (RT).

STM measurements. The STM topographic and spectroscopic experiments were conducted in a UHV low-temperature STM system (CreaTec) at liquid helium temperature. STM topographic images were acquired in

constant-current mode. The dI/dV spectra were measured using the standard lock-in technique with an 8 mV bias modulation of at 711.333 Hz. The STM tips were chemically etched tungsten tips and were spectroscopically calibrated against the Shockley surface states of cleaned Au(111) surfaces before being utilized on $SnSe_2$.

ARPES measurements. ARPES measurements were performed at the home-designed facility with a base pressure of better than 5×10^{-11} Torr and photon energy $\hbar\omega = 21.20$ eV, at a temperature below 80 K.

mPPE measurements. mPPE experiments were conducted in a UHV angle-resolved photoemission spectroscopy system that recorded spectra using a hemispherical electron energy analyzer (SPECS PHOIBOS 150) with a 2D delay-line detector (DLD). The base pressure of the system is better than 2×10^{-10} mbar. The hemispherical electron analyzer recorded 2D spectra of photoelectron counts vs. final state energy, E_{final}, and parallel momentum, $k_{//}$. A 3 V bias was applied between the sample and analyzer to collect near-zero kinetic energy electrons. The photon-excitation source for the mPPE measurements is a noncollinear parametric amplifier (NOPA) system pumped by a Light Conversion Pharos Impulse laser. The NOPA system operates at a power of approximately 10 μJ pulse^{-1} with a repetition rate of 1 MHz and a tunable wavelength in the range of 500–900 nm (photon energy of 2.48 to 1.38 eV). The NOPA outputs is compressed by multiple reflections from matched pairs of negative dispersion prisms to produce the shortest autocorrelation trace. The s- and p-polarized light is tuned by the rotation angle of a $\lambda/2$ waveplate. The excitation light with an incident angle of 45° from the surface normal is used, with a focused beam size of about 50 μm radius at the sample surface.

DFT calculation. Density Functional Theory (DFT) calculations were performed using the Vienna Ab initio Simulation package (VASP) [44, 45], employing the generalized gradient approximation with the Perdew–Burke–Ernzerhof (PBE) functional [46] for the exchange-correlation potential, and the projector augmented wave method. For bulk $SnSe_2$, the structures were fully relaxed until the residual force per atom was less than 0.02 eV/Å. Energy cutoffs for plane waves were set at 400 eV for the plane-wave-basis setting, and the Brillouin zone was sampled with a 9 × 9 × 4 Γ-centered k-point mesh. The PBE functional was employed in the electronic structure calculations based on the optimized atomic structures. For the band structure calculations of bulk $SnSe_2$, 40 $k_{//}$-points were sampled along each of the high symmetry lines in the Brillouin zone.

The transition dipole moments (TDM) are calculated as follows:

$$T_{n'n} = \langle \Psi_{n'} | \, \hat{\varepsilon} \cdot \boldsymbol{r} \, | \Psi_n \rangle \, .$$

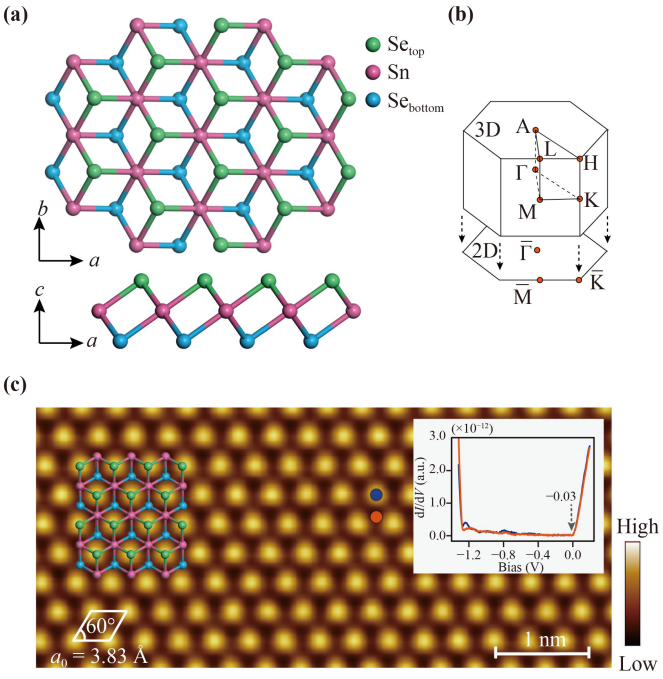

Fig. 1 **(a)** The top and side views of the atomic structure of 1T-$SnSe_2$. **(b)** Schematic representation of the 3D Brillouin zones of 1T-$SnSe_2$ along with its projection onto the (001) surfaces. **(c)** Typical STM topography image of the $SnSe_2$(001) surfaces acquired at a sample bias of 0.6 V and a tunneling current of 8 pA. The white rhomboid defines the unit cell of the surface. The atomic structural model of one $SnSe_2$ sandwich-layer on the surface illustrates that the bright contrast resolved by STM originates from the Se atoms on the top atomic layer. The inset shows typical STS dI/dV spectra acquired on the surfaces.

To compare with the experimental photoemission spectrum, the dipole moments are broadened with a Gaussian expansion. Since the experiments measure the excitation at Γ point, we only calculate the TDM at the Γ point. To include the IPs in the TDM calculations, we used 10-layer $SnSe_2$ slab model to obtain the wavefunction of the states, and a 20-Å vacuum layer included in the calculations to separate the periodic images of the slab.

3 Results and discussion

As shown in Fig. 1(a), $SnSe_2$ crystallizes in a layered structure of Se–Sn–Se sheets with octahedral Sn coordination [47–50]. $SnSe_2$ exhibits a rich polytypism which results from the various stacking sequences of identical Se–Sn–Se layers. The most common polytype contains one formula unit per unit cell and belongs to space group 164 [51], which is usually referred to as 1T with "1" referring to the number of Se–Sn–Se minimal sandwiches [52–54].

Figure 1(b) shows the three-dimensional (3D) Brillouin zone of 1T-$SnSe_2$ with high symmetry points and its 2D

projection onto (001) surfaces. Our self-grown $SnSe_2$ crystals were characterized with X-ray diffraction (XRD) [Fig. S1 of the Electronic Supplementary Materials (ESM)], where the sharp (001) diffraction peaks confirm 1*T*-$SnSe_2$ single crystals. The atomically resolved STM image [Fig. 1(c)] taken on the *in-situ* cleaved 1*T*-$SnSe_2$ surfaces shows a hexagonal lattice structure. The resolved bright spots correspond to Se atoms in top Se layers [55, 56]. The measured lattice constant (a_0) of 3.83 ± 0.03 Å is consistent with previous reports [55–57]. Typical scanning tunneling dI/dV spectra taken on the bright and dark contrasts on the surface [inset in Fig. 1(c)] exhibit semiconducting characters, with the conduction band minimum (CBM) crossing E_F. This indicates a slightly *n*-doped 1*T*-$SnSe_2$, a finding further confirmed by our ARPES measurement (Fig. S2 of the ESM), which shows an occupied CBM at M point with a binding energy of –0.03 eV relative to E_F. ARPES also reveals the valence band maximum (VBM) of –1.30 eV at Γ. This establishes an indirect band gap of approximately 1.30 eV, consistent with our tunneling spectra results. A recent ARPES studies on a 69-layers 1*T*-$SnSe_2$ thin films grown on n^+-GaAs(111) substrates show similar results [57].

While the occupied electronic structure of 1*T*-$SnSe_2$ has been detected, the unoccupied electronic states have not yet been probed. With the aim of directly resolving the unoccupied electronic states and investigating possible excitation between the occupied and unoccupied states, we conducted mPPE measurements on our grown 1*T*-$SnSe_2$ samples. In Fig. 2(a), we present the photoelectron yield along the surface normal for *p*-polarized (p_{in}) incident radiation with different central energies varying from 1.65 to 2.25 eV (photon energy $\hbar\omega$). The final-state energy (E_{final}) of the electrons is measured with respect to E_F. In Fig. 2(a), our spectra clearly exhibit well-resolved features that shift as we vary the photon energy. This is in stark contrast to non-photoelectric electron emissions, which are insensitive to the band structure of the irradiated solids and results in structureless spectra [17, 19]. Therefore, our spectra are primarily contributed by the photoelectric effect, and the observed features can be unambiguously interpreted on the basis of band structure effects. By identifying the low-energy cut-off of the spectra in Fig. 2(a), which corresponds to the vacuum level (E_V), we determined the work function Φ of bulk 1*T*-$SnSe_2$ by $\Phi = E_V - E_F = 5.40$ eV. This value is close to the measured electron affinity of 5.20 eV for $SnSe_2$ thin films in heterostructures composed of epitaxial layers of $SnSe_2$ on WSe_2, MoS_2, $MoTe_2$ and GaSe substrates [58, 59].

In the mPPE spectra, three separate features, labeled I, II and III [as marked in Fig. 2(a)], can be identified. These features evolve into an overwhelming peak feature at most photon energies. Peaks I, II and III exhibit noticeable dispersion with changing photon energies, as clearly demonstrated in the insets of Fig. 2(a). This shift with $\Delta\hbar\omega$ could be understood in the following scenario: In a mPPE process (generally non-resonant) involving states with fixed energy (i.e., not dispersing with $k_\perp$), as is the case of $SnSe_2$ due to weak van der Waals (vdW) interlayer interactions, it can be expected that the peak position from the initial state tunes with $m\Delta\hbar\omega$, the first intermediate state with $(m–1)\Delta\hbar\omega$, the second intermediate state with $(m–2)\Delta\hbar\omega$, and so on [60]. Plotting E_{final} versus photon energy in Fig. 2(b) reveals three different linear dispersions: peak I tunes with a slope of $4\Delta\hbar\omega$, peak II with $2\Delta\hbar\omega$ and peak III with $1\Delta\hbar\omega$. This implies that a 4PPE process might occur in the observations. Accordingly, electrons on these peaks are emitted out by the adsorption of 4, 2, and 1 photons, resulting in their binding energies. Using the formula $E_{binding} = E_{final} - n\hbar\omega$ (where n equals the number of additional photons necessary to reach the final state), the binding energies are calculated to be –1.28, +2.65 and +4.60 eV, respectively. In the following, we refer to the electronic states associated with features I, II and III as States I, II and III for convenience. Furthermore, Fig. 2(b) shows an intersection at $\hbar\omega = 1.94$ eV between the fitting lines for States I, II, III. This suggests the possible potential occurrence of a resonant 4PPE process that might involves States I, II, III as the initial state, second and third intermediate state, respectively. This implication is supported by the highest intensity of the dominant peak at 1.94 eV (the cyan curve) in Fig. 2(a). As will be explained in details below, the existence of resonant 4PPE is further confirmed later with the band-structure results of $SnSe_2$.

Since photons in the visible and UV range cannot impart significant momentum to electrons, multiphoton photoexcitation effectively proceeds vertically within the electronic $E(k_{//})$ band-structure. This property enables the determination of the separation of electronic bands at specific k points by identifying resonances between multiple states coupled by the incident radiation. This approach allows us to assign the observed states in the band-structure of $SnSe_2$. The assignment of the various features in our spectra is performed with reference to Fig. 2(c), which presents the electronic structure of bulk $SnSe_2$ for the $k_{//}$-space lines (Γ–M and Γ–K lines) relevant to emission along the surface normal of a $SnSe_2$(001) surface. Figure 2(c) is consistent with the reported results [57, 61], and we have marked key points, including the maximum of the valence band (VBM, –1.05 eV at the Γ point); the minimum of the first conduction band ($CB1_M$, –0.03 eV at the M point); the first conduction band ($CB1_\Gamma$, +0.20 eV at the Γ point) and the second conduction band (CB2, +2.15 eV at the Γ point). The VB bands consist of energetically closed d_{xy} and $d_{x^2-y^2}$ orbitals, which, according to our ARPES experiments (Fig. S2 of the ESM), cannot be resolved within the experimental resolution. ARPES results in Fig. S2 reveal

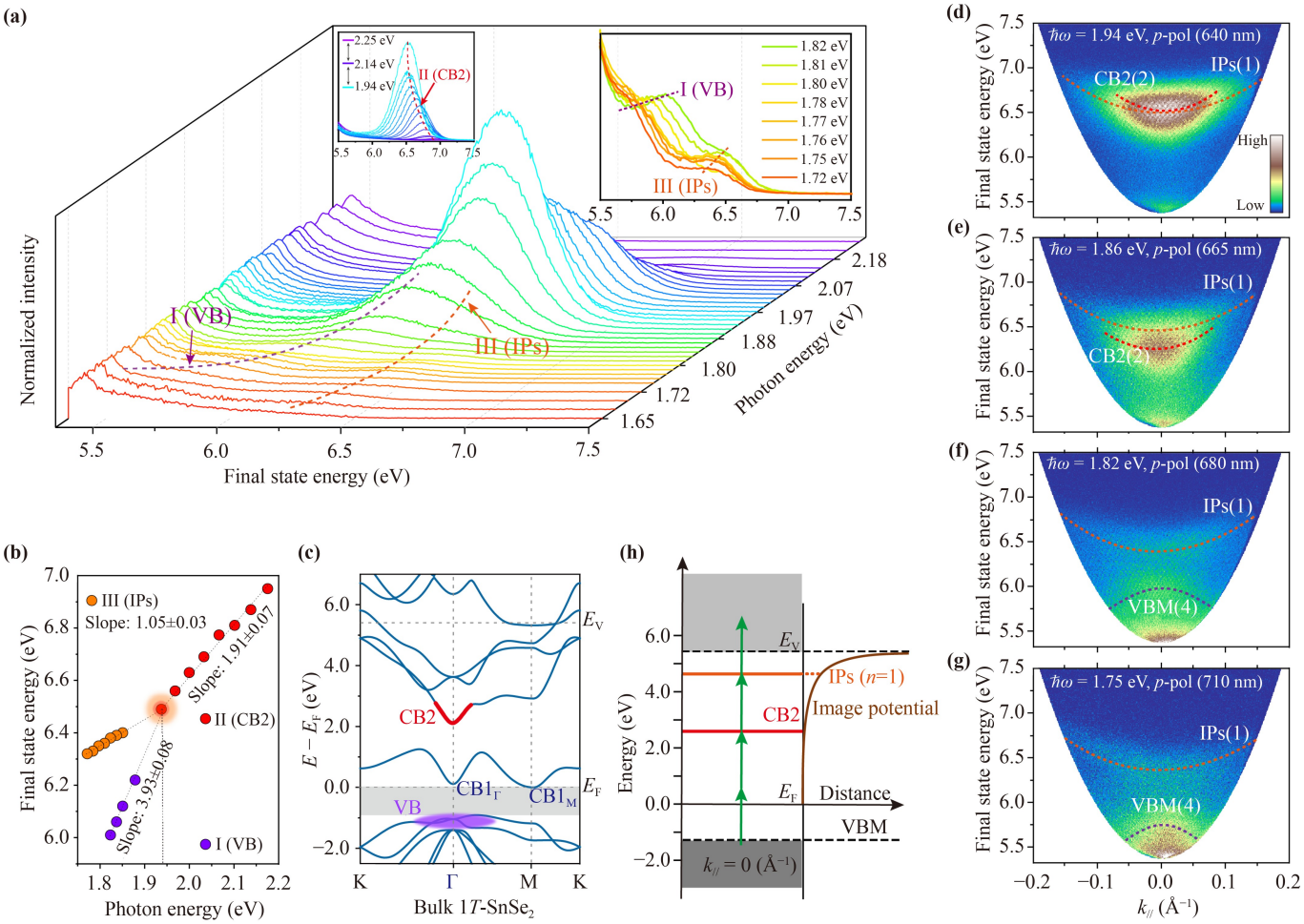

Fig. 2 **(a)** The normal-emission mPPE spectra versus photon energy measured with p-polarized irradiation from the $SnSe_2$(001) surfaces. Three separated features, labelled as I, II and III, are marked in the spectra. The insets highlight each of these features individually. **(b)** The peak positions of features I, II and III in the E_{final} versus photon energy plot. The dotted line represents the linear fitting of the data for VB, CB2, and IPs. **(c)** The calculated band structure along K–M–Γ–K of bulk 1T-$SnSe_2$, relevant to the normal emission geometry of the mPPE. CB2 and VB around Γ point are highlighted red and purple, respectively. **(d–g)** The 4PPE intensity versus $k_{//}$ along Γ–M with p-polarized incident radiation on $SnSe_2$ surfaces at different irradiation photon energies. CB2, IPs, and VB are fitted using red, orange and purple parabolic dashed lines, respectively. **(h)** Schematic representation of band structure alignment at Γ point with the proposed 4PPE resonance for a photon energy near 1.94 eV.

a VB signal which is flat around Γ and spans the energy window from –1.35 to –2.10 eV, consistent with the DFT calculations. A similar VB was also observed by ARPES in a 69-layers 1T-$SnSe_2$ thin films [57], providing occupied initial states with variable binding energies that do not exhibit a strong dependence on $k_{//}$ near Γ. ARPES results also show a very weak occupied CB close to M, corresponding to the DFT-observed $CB1_M$. However, $CB1_M$ is not considered as an initial state because it is located at the M point. $CB1_\Gamma$ and CB2 are absent in ARPES observations as they are unoccupied. The population of $CB1_\Gamma$ and CB2 from occupied VB initial states would be expected in mPPE. It is worth noting that $CB1_\Gamma$ cannot be reached resonantly with the photon energies in our experiment because photon energies near 1.70 eV are non-resonant with respect to the VB and $CB1_\Gamma$. Furthermore, we observe that CB2 bands are nearly symmetric within the experimentally observable $k_{//}$ rang along Γ–M and Γ–K, resulting in indistinguishable photoelectron emission from these two $k_{//}$-space lines. This symmetry is confirmed in experiments as mPPE spectra do not exhibit noticeable differences when the sample is rotated in the surface plane. Therefore, we can analyze the mPPE data by considering only one $k_{//}$-space line, i.e., the Γ–M line.

As is commonly understood, theoretical band structures often do not quantitatively match experimental photoemission data. However, a reasonable assumption is that the absolute values for critical points can be adjusted to align with known experimental data, ensuring that the

calculations correctly depict the dispersion of the bands. To facilitate a more accurate comparison with the theoretical band structure, we present in the mPPE spectral images of E_{final} vs. parallel momentum ($k_{//}$) along Γ–M with p-polarized light Figs. 2(d)–(g). These images reveal information about the dispersions of the bands associated with State I, II, III. At a photon energy of $\hbar\omega$ = 1.94 eV [Fig. 2(d)], we observed an upward-dispersed feature with very high intensity, possibly attributed to the resonance involving States I, II and III. As the excitation photon energy decreases to 1.86 eV, two upward-dispersive bands corresponding to States II and III evolve. These bands are fitted and overlaid by the orange and red parabolic dashed lines, respectively [Fig. 2(e)]. Furthermore, as the photon energy decreases further to 1.82 eV, the band related State II fades away, while the band associated with State I emerges with a downward dispersion, depicted by the purple parabolic dashed line in Fig. 2(f). Simultaneously, the band related to State III is almost isolated, exhibiting an upward parabolic dispersion. Both the bands related with States I and III become more clearly resolved at $\hbar\omega$ = 1.75 eV [Fig. 2(g)]. These results confirm an unambiguous downward dispersion for the band related to State I, an upward dispersion for the band related to State III, and a possible upward dispersion for the band related to State II.

By combining the established energies levels and dispersions for States I, II and III in mPPE, with the band-structure results shown in Fig. 2(c), we can readily assign State I (–1.28 eV) as originating from the VB band (calculated at –1.05 eV) and State II (+2.65 eV) as originating from the CB2 band (calculated value at +2.15 eV). The quantitative energy level discrepancies between the experiment and theory may be partially attributed to the fact that the calculation was performed for neutral $SnSe_2$, whereas the measurements were conducted on a slightly n-doped sample, as confirmed by STS and ARPES spectra. The missing counterpart for State III in the bulk band-structure depicted in Fig. 2(c) is identified as the n = 1 image potential states (IPs), which are present in the calculated band structure of a 10-layers $SnSe_2$ (as shown in Fig. S3 of the ESM) due to the presence of surfaces. Basing the observed results, we present a schematic representation of the band levels at Γ in Fig. 2(h) to explore k-conserving resonance in the band structure as a function of photon energy. According to the relative energy separation between VB, CB2 and IPs, a 4PPE resonant multiphoton transition is indeed possible for $\hbar\omega$ = 1.94 eV [as indicated by dashed lines in Fig. 2(d)]. The highest peak at $\hbar\omega$ = 1.94 eV in Fig. 2(a) can be attributed to a direct excitation process: VB → CB2 → IPs → E_{final}. In the first step, electrons are resonantly excited from the occupied VB band to CB2 through the adsorption of two photons. In the second step, resonant excitation populates the n = 1 IPs at 4.60 eV above E_{F}. In the final step, electrons are photoemitted at an energy of 6.54 eV.

Considering that the photoemission count rate of a 4PPE process is diminished by about four orders of magnitude compared to that of 1PPE, the observed significant 4PPE intensity at 6.54 eV is remarkable. Winkelmann *et al.* [7] have reported a 3PPE process on Cu(001) surfaces, beginning with Cu d bands and involving the unoccupied sp band and the n = 1 IPs. This 3PPE process was found to be highly efficient, producing a signal higher in intensity than the simultaneously observed 2PPE signal, which occurs through non-resonant pathways [7]. These results emphasize the importance of double resonances in the VB → CB2 → IPs → E_{final} 4PPE process in determining the high photoemission yield.

To investigate this further, we deliberately switched the incident p_{in} radiation to s-polarized (s_{in}) radiation, where the IPs would not be populated due to a matrix element effect [3], as determined by the geometry of s_{in} radiation [see Fig. 3(c)]. In this configuration, the only $k_{//}$ conserving transition from the intermediate CB2 to the final photoemitted state is a non-resonant two-photon process. This effectively eliminates the resonance of CB2 → IPs, and the excitation from CB2 to the final state can be understood through a virtue state, as depicted in Figs. 3(a) and (b) respectively. The 4PPE results upon p_{in} and s_{in} polarized radiations at 1.94 eV are presented in Figs. 3(d) and (e), respectively. Under s-polarization, the prominent, high-intensity, upward-dispersed feature observed under p-polarization transforms into a faint, upward-dispersed feature with very limited $k_{//}$ around the Γ point. We attribute this signal to CB2, which is populated by resonant excitation from VB vias adsorption of two photons and then is excited non-resonantly to E_{final} through the adsorption of another two photons. The reason CB2 is observed in a very limited $k_{//}$ range might be due to the parabolic dispersion of CB2 detuning the resonance from the "non-dispersing" VB around Γ. As the weaker feature in the s_{in} results share the same resonant VB → CB2 transition as in the p_{in} results, the transitions of VB → CB2 and CB2 → IPs have low yields if they contribute separately to the excitation. Therefore, the double resonance from the VB → CB2 → IPs is the primary factor resulting in the substantial 4PPE p_{in} yield at 6.54 eV. By presenting the normalized 4PP spectral line profiles at $k_{//}$ = 0 Å^{-1} in Figs. 3(d) and (e), it is evident that the photoelectron yield at 6.54 eV for p_{in} radiation is almost 40 times higher than that for s_{in} radiation. Although further work is needed to quantitatively understanding this factor, the discovery of double resonances involving both the bulk and surface electronic states of $SnSe_2$ could contribute exploring its related optoelectronic applications, such as photodetectors [47–50].

The enhanced photoelectron yield of resonant 4PPE

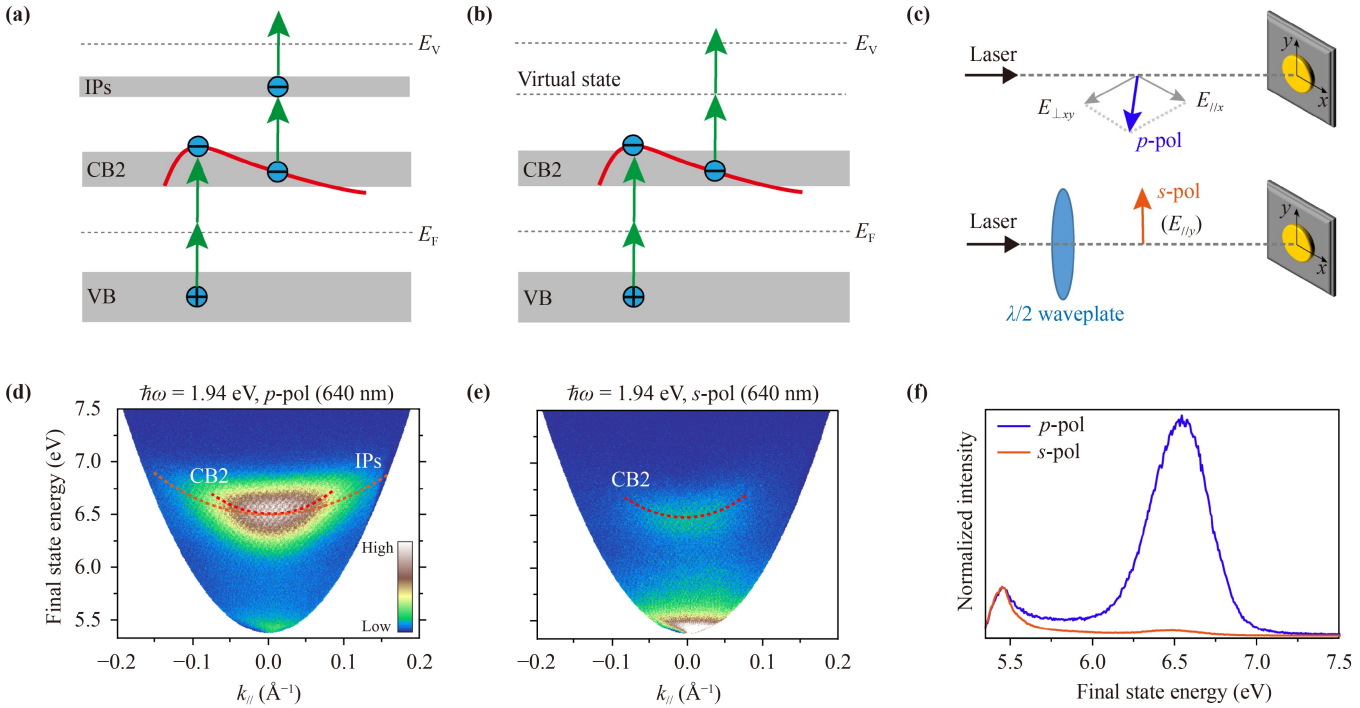

Fig. 3 **(a)** Schematic illustration of the double-resonant 4PPE process of VB → CB2 → IPs → E_{final}, where the IPs serves as the second intermediate state. **(b)** Schematic illustration of the VB → CB2 → Vs (virtual state) → E_{final} 4PPE process, in which the IPs is replaced by a virtual state. In this case, there is no resonance between CB2 with the second intermediate state. **(c)** The experimental geometry of *p*- and *s*-polarized irradiations. *s*-polarized irradiation contains only the in-plane ($E_{//y}$) electric field, while the *p*-polarized light includes both the in-plane ($E_{//x}$) and out-of-plane ($E_{\perp xy}$) components. **(d, e)** The 4PPE intensity versus $k_{//}$ along Γ–M with *p*- and *s*-polarized incident radiation on $SnSe_2$ surfaces respectively, at a photon energy of 1.94 eV. CB2 and IPs are represented by red and orange parabolic dashed lines, respectively. **(f)** Normal-emission 4PPE spectra measured with *p*-polarized (blue) and *s*-polarized (yellow) irradiations from the $SnSe_2$ surfaces, corresponding to $k_{//} = 0$ Å^{-1} in (d) and (e), respectively. The spectra are normalized according to the work function edge.

further is further confirmed by DFT calculations. Initially, we visualize the wavefunction normal ($|\psi|^2$) of VB, CB2 and $n = 1$ IPs, as shown in Figs. 4(a)–(c). Notably, the wavefunction of VB exhibits even (+) parity, whereas CB2 displays odd (–) parity according to the inversion center of $SnSe_2$ crystalline structure, indicating a permitted transition between the two states [62]. We proceed to calculate the transition dipole element (TDM), denoted as $T_{n'n} = \langle \Psi_{n'} | \hat{\varepsilon} \cdot \boldsymbol{r} | \Psi_n \rangle$, for VB → CB2, CB2 → IPs and VB → IPs, as presented in Fig. 4(d). It is evident that $T_{VB\to CB2} > T_{CB2\to IPs} > T_{VB\to IPs}$, with a difference spanning two orders of magnitude. The significant TDM from VBM to CB2 can be attributed to the wavefunction distributions illustrated in Figs. 4(a) and (b). The outcome of $T_{CB2\to IPs} > T_{VBM\to IPs}$ can be ascribed to the relatively greater out-of-plane distribution of CB2 wavefunction compared to VB. This discrepancy arises because the transition between CB2/VB and IPs is primarily determined by the wavefunction overlap in the out-of-plane direction. CB2 contributes more to the p_z and d_{z^2} orbitals, while VB has a higher contribution from p_{xy}, d_{xy}, $d_{x^2-y^2}$ orbitals. The transition efficiency of VB → CB2 → IPs can be estimated by $T_{VB\to CB2}$* $T_{CB2\to IPs}$, which is significantly larger than that of VB → IPs ($T_{VB\to IPs}$). These theoretical findings highlight that resonant excitation through the real CB2 intermediate state greatly enhances the excitation efficiency between the initial VB and intermediate IPs, thus supporting the experimental observation of the substantial 4PPE signals though the double-resonant pathways.

4 Conclusion

By demonstrating the contribution of resonant excitation pathways in 4PPE from $SnSe_2$(001), we identify dominant features in the photoelectron spectra originating from VB, CB2, and IPs of $SnSe_2$. The identification is validated by comparing them with the DFT calculated band structure of $SnSe_2$(001). Based on *p*- and *s*-polarized photoemission spectra, double-resonant 4PPE from VB → CB2 → IPs → E_{final} exhibits a significantly enhanced photoemission yield when compared to the single-resonant VB → CB2 → Vs (virtual state) → E_{final} process, where the IPs is replaced by a virtual state. The experimental results align with DFT calculations, which

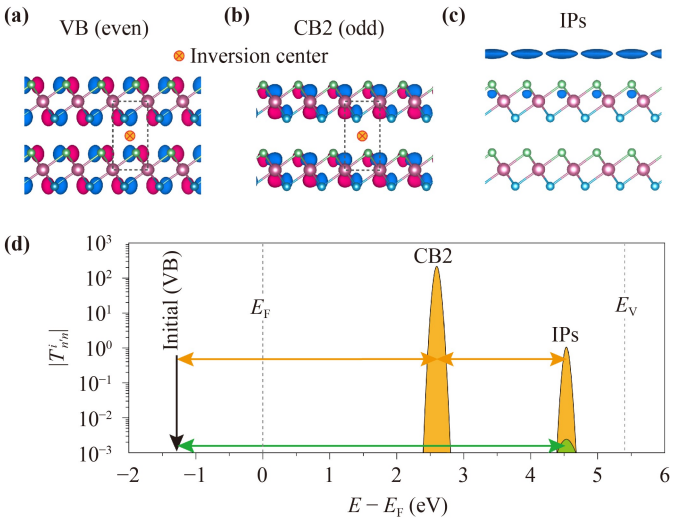

Fig. 4 **(a–c)** The side view of the wavefunction normal ($|\psi|^2$) of VB, CB2, and $n = 1$ IPs. The parity of $|\psi|^2$ is even (+) for VB and odd (−) for CB2 according to the inversion center, as highlighted by the black-dashed rectangle. **(d)** The calculated transition dipole moment $|T^i_{n'n}|$ (broadened with Gaussian functions) of VB → CB2, CB2 → IPs, and VB → IPs. The energy is relative to E_F.

suggest that resonant excitation involving real electronic state as intermediate state can substantially enhance the excitation efficiency between the initial and final states. While 2PPE has significantly contributed to the understanding of electronic structure and ultrafast electron dynamics at solid surfaces [1, 3–5, 63–65], similar studies of higher-order mPPE have just begun and have primarily focused on metals [6–9]. Our findings suggest extensions to future mPPE studies in mapping unoccupied electronic structure of 2D semiconductors, exploring multiphoton resonance between occupied/unoccupied bulk and unoccupied surface states, and studying the quantum coherence of the resonant excitation pathways through interferometric measurements [9, 12, 13].

Declarations The authors declare that they have no competing interests and there are no conflicts.

Author contributions C.X.J. and K.H. performed mPPE measurements. H.L.G. and K.H. performed first-principles calculations. X.X.C., Q.Y., C.C.L. assisted with the STM measurements. C.L.W. and N.X. performed ARPES measurements. G.Q.M. and L.M.C. grew the $SnSe_2$ single crystals. M.F. and L.M.C. initiated the project and experiments. M.F. and L.M.C. analyzed the data and wrote the manuscript with input from all authors.

Data availability The data that support the findings of this study are available from the corresponding authors upon request.

Electronic supplementary materials The online version contains supplementary material available at https://doi.org/10.1007/s11467-023-1365-4 and https://journal.hep.com.cn/fop/EN/10.1007/s11467-023-1365-4.

Acknowledgements We gratefully acknowledge the productive discussions with Shijing Tan, Xuefeng Cui and Hrvoje Petek. This work was supported by the Strategic Priority Research Program of the Chinese Academy of Sciences (Grant No. XD30000000), the National Key R&D Program of China (Grant Nos. 2018YFA0305802 and 2017YFA0303500), and the National Natural Science Foundation of China (Grant No. 11774267). Calculations were performed at the supercomputing center of WHU of China.

References

1. H. Petek and S. Ogawa, Femtosecond time-resolved two-photon photoemission studies of electron dynamics in metals, *Prog. Surf. Sci.* 56(4), 239 (1997)
2. T. Fauster, M. Weinelt, and U. Höfer, Quasi-elastic scattering of electrons in image-potential states, *Prog. Surf. Sci.* 82(4–6), 224 (2007)
3. K. Giesen, F. Hage, F. Himpsel, H. Riess, and W. Steinmann, Two-photon photoemission via image-potential states, *Phys. Rev. Lett.* 55(3), 300 (1985)
4. R. Schoenlein, J. G. Fujimoto, G. Eesley, and T. Capehart, Femtosecond studies of image-potential dynamics in metals, *Phys. Rev. Lett.* 61(22), 2596 (1988)
5. C. Waldfried, D. McIlroy, J. Zhang, P. Dowben, G. Katrich, and E. W. Plummer, Determination of the surface Debye temperature of Mo(112) using valence band photoemission, *Surf. Sci.* 363(1–3), 296 (1996)
6. F. Bisio, A. Winkelmann, C. Chiang, H. Petek, and J. Kirschner, Band structure effects in above threshold photoemission, *J. Phys.: Condens. Matter* 23(48), 485002 (2011)
7. A. Winkelmann, W. C. Lin, C. T. Chiang, F. Bisio, H. Petek, and J. Kirschner, Resonant coherent three-photon photoemission from Cu(001), *Phys. Rev. B* 80(15), 155128 (2009)
8. F. Bisio, M. Nývlt, J. Franta, H. Petek, and J. Kirschner, Mechanisms of high-order perturbative photoemission from Cu(001), *Phys. Rev. Lett.* 96(8), 087601 (2006)
9. M. Reutzel, A. Li, Z. Wang, and H. Petek, Coherent multidimensional photoelectron spectroscopy of ultrafast quasiparticle dressing by light, *Nat. Commun.* 11(1), 2230 (2020)
10. Y. Lin, Y. Li, J. T. Sadowski, W. Jin, J. I. Dadap, M. S. Hybertsen, and Osgood, Excitation and characterization of image potential state electrons on quasi-free-standing graphene, *Phys. Rev. B* 97(16), 165413 (2018)
11. A. A. Ünal, C. Tusche, S. Ouazi, S. Wedekind, C. T. Chiang, A. Winkelmann, D. Sander, J. Henk, and J. Kirschner, Hybridization between the unoccupied Shockley surface state and bulk electronic states on Cu(111), *Phys. Rev. B* 84(7), 073107 (2011)
12. H. Petek, A. Li, X. Li, S. Tan, and M. Reutzel, Plasmonic decay into hot electrons in silver, *Prog. Surf. Sci.* 98(3), 100707 (2023)
13. M. Reutzel, A. Li, and H. Petek, Coherent two-dimensional

multiphoton photoelectron spectroscopy of metal surfaces, *Phys. Rev. X* 9(1), 011044 (2019)
14. S. Ogawa and H. Petek, Two-photon photoemission spectroscopy at clean and oxidized Cu(110) and Cu(100) surfaces, *Surf. Sci.* 363(1–3), 313 (1996)
15. S. Luan, R. Hippler, H. Schwier, and H. Lutz, Electron emission from polycrystalline copper surfaces by multi-photon absorption, *Europhys. Lett.* 9(5), 489 (1989)
16. W. Fann, R. Storz, and J. Bokor, Observation of above-threshold multiphoton photoelectric emission from image-potential surface states, *Phys. Rev. B* 44(19), 10980 (1991)
17. S. Irvine, A. Dechant, and A. Elezzabi, Generation of 0.4-keV femtosecond electron pulses using impulsively excited surface plasmons, *Phys. Rev. Lett.* 93(18), 184801 (2004)
18. I. Kinoshita, T. Anazawa, and Y. Matsumoto, Surface and image-potential states on Pt(111) probed by two- and three-photon photoemission, *Chem. Phys. Lett.* 259(3–4), 445 (1996)
19. J. Kupersztych, P. Monchicourt, and M. Raynaud, Ponderomotive acceleration of photoelectrons in surface-plasmon-assisted multiphoton photoelectric emission, *Phys. Rev. Lett.* 86(22), 5180 (2001)
20. S. Tan, A. Argondizzo, C. Wang, X. Cui, and H. Petek, Ultrafast multiphoton thermionic photoemission from graphite, *Phys. Rev. X* 7(1), 011004 (2017)
21. S. Tan, Y. Dai, S. Zhang, L. Liu, J. Zhao, and H. Petek, Coherent electron transfer at the Ag/graphite heterojunction interface, *Phys. Rev. Lett.* 120(12), 126801 (2018)
22. S. Tan, L. Liu, Y. Dai, J. Ren, J. Zhao, and H. Petek, Ultrafast plasmon-enhanced hot electron generation at Ag nanocluster/graphite heterojunctions, *J. Am. Chem. Soc.* 139(17), 6160 (2017)
23. C. A. Formstone, E. T. FitzGerald, D. O'Hare, P. A. Cox, M. Kurmoo, J. W. Hodby, D. Lillicrap, and M. Goss-Custard, Observation of superconductivity in the organometallic intercalation compound $SnSe_2\{Co(\eta\text{-}C_5H_5)_2\}_{0.33}$, *J. Chem. Soc. Chem. Commun.* 0(6), 501 (1990)
24. C. A. Formstone, M. Kurmoo, E. T. FitzGerald, P. A. Cox, and D. O'Hare, Single-crystal conductivity study of the tin dichalcogenides $SnS_{2-x}Se_x$ intercalated with cobaltocene, *J. Mater. Chem.* 1(1), 51 (1991)
25. D. O'Hare, H. V. Wong, S. Hazell, and J. W. Hodby, Relatively isotropic superconductivity at 8.3 K in the Lamellar organometallic intercalate $SnSe_2\{Co(\eta\text{-}C_5H_5)_2\}_{0.3}$, *Adv. Mater.* 4(10), 658 (1992)
26. Z. Li, Y. Zhao, K. Mu, H. Shan, Y. Guo, J. Wu, Y. Su, Q. Wu, Z. Sun, A. Zhao, X. Cui, C. Wu, and Y. Xie, Molecule-confined engineering toward superconductivity and ferromagnetism in two-dimensional superlattice, *J. Am. Chem. Soc.* 139(45), 16398 (2017)
27. G. R. Bhimanapati, Z. Lin, V. Meunier, Y. Jung, J. Cha, S. Das, D. Xiao, Y. Son, M. S. Strano, V. R. Cooper, L. Liang, S. G. Louie, E. Ringe, W. Zhou, S. S. Kim, R. R. Naik, B. G. Sumpter, H. Terrones, F. Xia, Y. Wang, J. Zhu, D. Akinwande, N. Alem, J. A. Schuller, R. E. Schaak, M. Terrones, and J. A. Robinson, Recent advances in two-dimensional materials beyond graphene, *ACS Nano* 9(12), 11509 (2015)
28. R. A. Klemm, Pristine and intercalated transition metal dichalcogenide superconductors, *Physica C* 514, 86 (2015)
29. X. Zhou, L. Gan, W. Tian, Q. Zhang, S. Jin, H. Li, Y. Bando, D. Golberg, and T. Zhai, Ultrathin $SnSe_2$ flakes grown by chemical vapor deposition for high-performance photodetectors, *Adv. Mater.* 27(48), 8035 (2015)
30. A. Giri, G. Park, and U. Jeong, Layer-structured anisotropic metal chalcogenides: Recent advances in synthesis, modulation, and applications, *Chem. Rev.* 123(7), 3329 (2023)
31. E. P. Mukhokosi, G. V. Manohar, T. Nagao, S. B. Krupanidhi, and K. K. Nanda, Device architecture for visible and near-infrared photodetectors based on two-dimensional $SnSe_2$ and MoS_2: A review, *Micromachines (Basel)* 11(8), 750 (2020)
32. X. Li, L. Li, H. Zhao, S. Ruan, W. Zhang, P. Yan, Z. Sun, H. Liang, and K. Tao, $SnSe_2$ quantum dots: Facile fabrication and application in highly responsive UV-detectors, *Nanomaterials (Basel)* 9(9), 1324 (2019)
33. E. Mooser and W. B. Pearson, New semiconducting compounds, *Phys. Rev.* 101(1), 492 (1956)
34. G. Domingo, R. S. Itoga, and C. R. Kannewurf, Fundamental optical absorption in SnS_2 and $SnSe_2$, *Phys. Rev.* 143(2), 536 (1966)
35. M. Y. Auyang and M. L. Cohen, Electronic structure and optical properties of SnS_2 and $SnSe_2$, *Phys. Rev.* 178(3), 1279 (1969)
36. R. Williams, R. Murray, D. Govan, J. Thomas, and E. Evans, Band structure and photoemission studies of SnS_2 and $SnSe_2$. I. Experimental, *J. Phys. C Solid State Phys.* 6(24), 3631 (1973)
37. R. Cohen, G. Wertheim, A. Rosencwaig, and H. Guggenheim, Multiplet splitting of the 4s and 5s electrons of the rare earths, *Phys. Rev. B* 5(3), 1037 (1972)
38. G. Domingo, R. Itoga, and C. Kannewurf, Fundamental optical absorption in SnS_2 and $SnSe_2$, *Phys. Rev.* 143(2), 536 (1966)
39. C. Fong and M. Cohen, Electronic charge densities for two layer semiconductors – SnS_2 and $SnSe_2$, *J. Phys. C Solid State Phys.* 7(1), 107 (1974)
40. J. George and K. Joseph, Absorption edge measurements in tin disulphide thin films, *J. Phys. D Appl. Phys.* 15(6), 1109 (1982)
41. M. Schlüter and M. L. Cohen, Valence-band density of states and chemical bonding for several non-transition-metal layer compounds: $SnSe_2$, PbI_2, BiI_3, and GaSe, *Phys. Rev. B* 14(2), 424 (1976)
42. A. Smith, P. Meek, and W. Liang, Raman scattering studies of SnS_2 and $SnSe_2$, *J. Phys. C Solid State Phys.* 10(8), 1321 (1977)
43. R. Schlaf, C. Pettenkofer, and W. Jaegermann, Band lineup of a $SnS_2/SnSe_2/SnS_2$ semiconductor quantum well structure prepared by van der Waals epitaxy, *J. Appl. Phys.* 85(9), 6550 (1999)
44. G. Kresse and J. Furthmüller, Efficient iterative schemes for *ab initio* total-energy calculations using a plane-wave basis set, *Phys. Rev. B* 54(16), 11169 (1996)
45. G. Kresse and J. Furthmüller, Efficiency of *ab-initio* total energy calculations for metals and semiconductors

using a plane-wave basis set, *Comput. Mater. Sci.* 6(1), 15 (1996)

46. J. P. Perdew, K. Burke, and M. Ernzerhof, Generalized gradient approximation made simple, *Phys. Rev. Lett.* 77(18), 3865 (1996)
47. M. A. Franzman, C. W. Schlenker, M. E. Thompson, and R. L. Brutchey, Solution-phase synthesis of SnSe nanocrystals for use in solar cells, *J. Am. Chem. Soc.* 132(12), 4060 (2010)
48. L. Li, Z. Chen, Y. Hu, X. Wang, T. Zhang, W. Chen, and Q. Wang, Single-layer single-crystalline SnSe nanosheets, *J. Am. Chem. Soc.* 135(4), 1213 (2013)
49. C. Zhang, H. Yin, M. Han, Z. Dai, H. Pang, Y. Zheng, Y. Q. Lan, J. Bao, and J. Zhu, Two-dimensional tin selenide nanostructures for flexible all-solid-state supercapacitors, *ACS Nano* 8(4), 3761 (2014)
50. X. Zhou, L. Gan, W. Tian, Q. Zhang, S. Jin, H. Li, Y. Bando, D. Golberg, and T. Zhai, Ultrathin $SnSe_2$ flakes grown by chemical vapor deposition for high-performance photodetectors, *Adv. Mater.* 27(48), 8035 (2015)
51. Y. Zhou, B. Zhang, X. Chen, C. Gu, C. An, Y. Zhou, K. Cai, Y. Yuan, C. Chen, H. Wu, R. Zhang, C. Park, Y. Xiong, X. Zhang, K. Wang, and Z. Yang, Pressure-induced metallization and robust superconductivity in pristine 1*T*-$SnSe_2$, *Adv. Electron. Mater.* 4(8), 1800155 (2018)
52. A. J. Forty, VI. The growth of cadmium iodide crystals (I): Dislocations and spiral growth, *Lond. Edinb. Dublin Philos. Mag. J. Sci.* 43(336), 72 (1952)
53. B. E. Brown and D. J. Beerntsen, Layer structure polytypism among niobium and tantalum selenides, *Acta Crystallogr.* 18(1), 31 (1965)
54. E. Bjerkelund and A. Kjkshus, On the structural properties of the $Ta_{1+x}Se_2$ phase, *Acta Chem. Scand.* 21, 513 (1967)
55. Y.-H. Mao, H. Shan, J.-R. Wu, Z.-J. Li, C.-Z. Wu, X.-F. Zhai, A.-D. Zhao, and B. Wang, Observation of pseudogap in $SnSe_2$ atomic layers grown on graphite, *Front. Phys.* 15(4), 43501 (2020)
56. Y. M. Zhang, J. Q. Fan, W. L. Wang, D. Zhang, L. Wang, W. Li, K. He, C. L. Song, X. C. Ma, and Q. K. Xue, Observation of interface superconductivity in a $SnSe_2$/epitaxial graphene van der Waals heterostructure, *Phys. Rev. B* 98(22), 220508 (2018)
57. E. B. Lochocki, S. Vishwanath, X. Liu, M. Dobrowolska, J. Furdyna, H. G. Xing, and K. M. Shen, Electronic structure of $SnSe_2$ films grown by molecular beam epitaxy, *Appl. Phys. Lett.* 114(9), 091602 (2019)
58. R. Schlaf, O. Lang, C. Pettenkofer, and W. Jaegermann, Band lineup of layered semiconductor heterointerfaces prepared by van der Waals epitaxy: Charge transfer correction term for the electron affinity rule, *J. Appl. Phys.* 85(5), 2732 (1999)
59. Q. Zhang, M. O. Li, E. B. Lochocki, S. Vishwanath, X. Liu, R. Yan, H. H. Lien, M. Dobrowolska, J. Furdyna, K. M. Shen, G. Cheng, A. R. Hight Walker, D. J. Gundlach, H. G. Xing, and N. V. Nguyen, Band offset and electron affinity of MBE-grown $SnSe_2$, *Appl. Phys. Lett.* 112(4), 042108 (2018)
60. W. Steinmann, Two-photon photoemission spectroscopy of electronic states at metal surfaces, *Phys. Status Solidi B* 192(2), 339 (1995)
61. J. M. Gonzalez and I. I. Oleynik, Layer-dependent properties of SnS_2 and $SnSe_2$ two-dimensional materials, *Phys. Rev. B* 94(12), 125443 (2016)
62. Y. Peter and M. Cardona, Fundamentals of Semiconductors: Physics and Materials Properties, Springer Science & Business Media, 2010
63. H. Petek, A. Heberle, W. Nessler, H. Nagano, S. Kubota, S. Matsunami, N. Moriya, and S. Ogawa, Optical phase control of coherent electron dynamics in metals, *Phys. Rev. Lett.* 79(23), 4649 (1997)
64. S. Ogawa, H. Nagano, H. Petek, and A. Heberle, Optical dephasing in Cu(111) measured by interferometric two-photon time-resolved photoemission, *Phys. Rev. Lett.* 78(7), 1339 (1997)
65. H. Petek, H. Nagano, and S. Ogawa, Hole decoherence of *d* bands in copper, *Phys. Rev. Lett.* 83(4), 832 (1999)